Advanced Composites and Hybrid Materials (2021) 4:1070–1081
https://doi.org/10.1007/s42114-021-00319-9

ORIGINAL RESEARCH

Investigations about the influence of different carbon matrixes on the electrochemical performance of $Na_3V_2(PO_4)_3$ cathode material for sodium ion batteries

Xiufang Dong[1] · Xiaolong Zhao[1] · Yanjun Chen[1] · Chao Wang[1]

Received: 15 June 2021 / Revised: 29 July 2021 / Accepted: 1 August 2021 / Published online: 15 September 2021

Abstract
Na superionic conductor (NASICON)–type $Na_3V_2(PO_4)_3$(NVP) has attracted great attention due to its unique conductive framework and high capacity. However, the poor intrinsic conductivity seriously restricted the further development. This work proposes an effective strategy of introducing the beneficial carbon-based matrix materials including reduced graphene oxide (rGO), polypyrrole (ppy), and carbon nanotubes (CNTs) to the NVP system. The modified composites reveal particular morphological features and enhanced specific surface areas, benefiting to improve the kinetic characteristics and sodium storage performance. Accordingly, the optimized NVP/C@CNT composite shows superior electrochemical performance. It can release a high reversible discharge capacity of 98.7 mAh g^{-1} at the 0.1 C rate. Meanwhile, a high capacity retention of 81% is obtained after 500 cycles at 2 C. Moreover, the kinetic characteristics demonstrate that the optimized NVP/C@CNT sample shows a high Na^+ diffusion coefficient. This work offers a unique avenue for the development of the modification and synthesis of polyanion cathodes for sodium ion batteries.

Keywords Carbon matrix · Electrochemical performance · $Na_3V_2(PO_4)_3$ · Cathode material · Sodium ion batteries

1 Introduction

Nowadays, energy crisis has been a serious issue around the world. The rapid development of new energy storage devices is a key scheme to solve the problem [1–13]. Lithium ion batteries (LIBs), possessing the high energy density, have been deemed to be the most successful commercial energy storage systems in the recent years [14–19]. Nevertheless, the drawbacks of raw-material limitation and uneven global distribution have boosted the costing price significantly [20–26]. Hence, the researchers have to explore more inexpensive alternatives with comparable performance. Sodium ion batteries (SIBs) have attracted much attention due to the low-cost raw materials and excellent electrochemical properties [27–32]. However, the larger radius of Na^+ (1.03 Å) and higher equivalent weight lead to sluggish kinetic characteristics during the charging and discharging processes [33–36]. Therefore, it is of great importance to investigate a promising electrode material with stable structure and superior kinetics.

In this regard, $Na_3V_2(PO_4)_3$(NVP) has been considered as a prospective cathode material with a unique Na superionic conductor (NASICON) framework, which can provide a facile channel for rapid transportation of Na^+ [36–38]. Moreover, the NVP composite can reveal a theoretical capacity of 117.6 mAh g^{-1} with a high voltage of 3.4 V, corresponding to the redox couple of V^{3+}/V^{4+} during the electrochemical procedure [38–40]. However, the poor intrinsic electronic conductivity seriously restricts the release of performance for the NVP system. Many efficient routes are proposed to improve the capability of electronic transportation of NVP material [41–48]. Among them, the most widely utilized method is recombining the conductive carbon-based matrix, such as carbon nanotubes and reduced graphene oxide [49–52].

In current work, we have modified the NVP composite by constructing a dual conductive framework containing the coated carbon layers and enwrapped carbon matrix materials. The optimized samples are synthesized by a facile sol–gel route. The investigation about the influence of

✉ Chao Wang
wangchao_nuc@126.com

[1] Advanced Energy Materials and Systems Institute, North University of China, Taiyuan 030051, China

different carbon matrixes on the crystal structure, morphological features, and sodium storage property for the NVP composite is conducted. As a result, the beneficial carbon matrix is facilitated to accelerate the migration of electrons and therefore significantly improve the rate capability of the electrodes. Distinctively, the NVP/C@CNT composite possesses the best electrochemical performance among all the samples. It can release reversible discharge capacities of 98.7, 89.3, 85.2, 83.2, 80.5, and 78.9 mAh g^{-1} at 0.1, 1, 2, 4, 6, and 10 C rates. A high capacity retention of 81% is obtained after 500 cycles at 2 C. Moreover, the kinetic characteristics conducted by CV measurement demonstrate the optimized NVP/C@CNT sample showing a high Na^+ diffusion coefficient (1.28×10^{-10} cm^2 s^{-1} for the charge process; 8.56×10^{-11} cm^2 s^{-1} for discharge process).

2 Experimental sections

2.1 Material preparation

All the samples were prepared by a facile sol–gel method. NH_4VO_3, citric acid, $NH_4H_2PO_4$, and Na_2CO_3 were utilized as raw materials. All the materials were original without other processing. Noteworthily, the addition of citric acid was an excess due to the complete reduction reaction of V^{5+}/V^{3+}. Moreover, the advantage citric acid can act as the chelating agent to form the favorable morphology, as well as providing the resources for coated carbon layers surrounding the active grains. Initially, the stoichiometric NH_4VO_3 and citric acid, $NH_4H_2PO_4$, and Na_2CO_3 were added into the deionized water to form a clarified solution with magnetic stirring. The precursor sample was heated at 80 °C until a gel was prepared. Subsequently, freeze-drying measurement was carried out to make the particles disperse uniformly. After this procedure, the black composites were grounded carefully and then preheated at 450 °C for 4 h in nitrogen atmosphere. Finally, the powders were sintered at 700 °C for 6 h at the same atmosphere. The optimized composites of $Na_3V_2(PO_4)_3$/C@CNTs, $Na_3V_2(PO_4)_3$/C@rGO, and $Na_3V_2(PO_4)_3$/C@ppy were synthesized by the same route except for the addition of CNTs, rGO, and ppy. Finally, the prepared $Na_3V_2(PO_4)_3$/C, $Na_3V_2(PO_4)_3$/C@CNTs, $Na_3V_2(PO_4)_3$/C@rGO, and $Na_3V_2(PO_4)_3$/C@ppy samples are abbreviated as NVP/C, NVP/C@CNTs, NVP/C@rGO, and NVP/C@ppy.

2.2 Characterization

X-ray diffraction measurement was conducted to investigate the crystal structure of all composites. The morphological features of all samples were determined by scanning electron microscopy (SEM, SU8010). The N_2 adsorption and desorption measurements were performed to obtain the surface area and pore size distribution (JWGB, BK122W). The carbon contents were determined by thermal gravimetric analysis (TG, METTLER).

2.3 Electrochemical measurements

The CR2016 type half-cells are used to evaluate the sodium storage properties of all composites. All coin cells are assembled in a glove box filled with argon. The electrode slurry was constituted by 80 wt% active material, 10 wt% conductive acetylene, and 10 wt% binder PVDF. N-Methyl-2-pyrrolidone (NMP) was utilized as the solvent solution. All the mixtures were ball-milled for 10 h to acquire the uniform slurry. Subsequently, an automatic coater was used to smear the obtained slurry onto a clean aluminum foil, which was dried in vacuum at 120 °C overnight. For matching the 2016 battery jar, we punched the electrode slice into disks with a diameter of 12 cm for the further package. As for a half-cell, sodium metal was used as the counter electrode, and Celgard 2400 membrane was utilized as the separator. The electrolyte contained 1 M $NaClO_4$ in propylene carbonate (PC) with 2 vol% fluoroethy-lene (FEC). The loading mass of active material in each electrode is 1.4 mg with a footprint area of 2.01 cm^{-2}. Cyclic voltammetry (CV) tests for all electrodes were explored on an electrochemical workstation (IVIUM-n-Stat). The measuring parameters are 2.3–4.1 V with various scan rates of 0.1, 0.2, 0.5, 1, 2, and 5 mV S^{-1}. Besides, a LAND Battery Testing System was carried out to evaluate the galvanostatic charge/discharge (GCD) processes in a scale of 2.3–4.1 V. Rate capability and cyclic performance of all samples were tested in the same system. All the measurements were conducted at room temperature.

3 Results and discussion

To investigate the effects of different carbon matrixes on the crystal structure, XRD measurements are explored and the results are revealed in Fig. 1. As shown below, all composites display sharp diffraction peaks within the range of 10–80°, indicating the excellent crystallinity for all samples. Obviously, the positions of peaks for all samples precisely correspond to the PDF card (#00–053-0018), revealing that the synthesized composites conform to the typical NVP system. Moreover, no obvious peaks representing impurities are observed, suggesting that the addition of the carbon matrix has no influence on the synthetic results. Furthermore, the peak shapes for all compounds (NVP@rGO, NVP@ppy, NVP@CNTs) are much sharper than those of the NVP/C sample, suggesting the better crystal stability for the carbon composites.

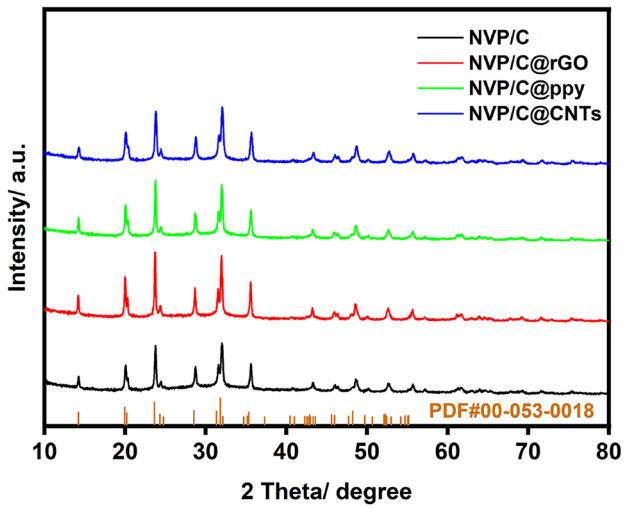

Fig. 1 XRD patterns of all samples

To deeply investigate the crystal structure and obtain the cell parameters, structural refinement is conducted by Highscore software and the results are revealed in Fig. 2 and Table 1. As shown in Fig. 2, the values of the fitting index (R) for all samples are very low, suggesting the reliability and veracity of the refined results. As presented in Table 1, there are no obvious changes to cell parameters including *a*, *c*, and *V* after combining with the carbon-based matrix materials. This is reasonable because the addition of carbon materials will not influence the internal crystal characteristics of the NVP system.

In order to explore the morphological features of all modified samples, SEM measurement is carried out and the results are revealed in Figs. 3. As shown in Fig. 3a, some lamellar rGO nanosheets embed into the irregular particles of NVP, isolating the contact between the active grains, which is beneficial to restricting the growth of NVP particles and therefore provide a shortened pathway for the migration of Na^+ and electrons. Meanwhile, as presented in Fig. 3d, some rGO sheets with a large surface can act as the matrix to support the adherence of active grains, supplying a favorable conductive network for facilitated transportation of electrons. Figure 3b displays the morphology of a ppy-decorated NVP/C sample, revealing that tubular ppy is utilized as the medium to connect the adjacent active NVP gains, showing a function of conducting the charge transfer between particles. The HRSEM image in Fig. 6e indicates that the pipe diameter of ppy is around 200 nm, and the length is more than 2 μm. Furthermore, the typical image of the CNT-enwrapped NVP/C sample is shown in Fig. 3c and f. Obviously, the agglomerated particle possesses a particle size of 5 μm, covered by a thin and uniform amorphous carbon layer. As can be seen in the HRSEM image with enlarged magnification (Fig. 3f), the big active grain is constituted of fine particles and massive conductive CNTs, in which CNTs wrap around the particle to construct the unique and efficient conductive framework. This mixed system significantly facilitates the transportation of Na^+ and electrons, resulting in the superior kinetic characteristics and electrochemical property. Similarly, all the carbon-based NVP/C composites show a phenomenon of particle clustering. This may be derived from the heat treatment at high temperature after the sol–gel method.

To deeply investigate the effects of adding carbon-based materials on the specific surface area, nitrogen isothermal adsorption/desorption tests are conducted and displayed in Fig. 4. As revealed in Fig. 4a, all plots of the four samples show typical-shape isotherms, indicating the identical IV curve with a hysteresis loop. This demonstrates that all samples possess the mesoporous microstructure [53, 54]. In addition, the specific surface area of NVP/C, NVP/C@rGO, NVP/C@ppy, and NVP/C@CNT composites is 21.812, 47.123, 32.287, and 58.535 $m^2\ g^{-1}$, respectively. Notably, combining with beneficial carbon-based matrix materials can significantly improve the surface area, resulting from the unique morphological features. Moreover, the enlarged area benefits to infiltrate the active electrode by electrolyte and provide sufficient space for the crystal volume shrinkage of NVP material during the charge/discharge process. Obviously, the NVP/C@CNT composite behaves the largest surface area among all samples, accompanied with a typical mesoporous structure, supplying the favorable capacitive charge storage and therefore improving the high-rate capability. Furthermore, Fig. 4b reveals the pore size distribution of all samples, further verifying the presence of mesopores. The average value of pore size is about 4 nm.

To investigate the carbon contents of all samples, thermal gravimetric (TG) analysis is conducted and the TG curves are patterned in Fig. 5. The numerical values of carbon content for the NVP/C sample is close to 4 wt%. Contents of NVP/C@CNTs, NVP/C@rGO, and NVP/C@ppy are 10.70 wt%, 9.51 wt%, and 12.01 wt%, respectively, which are much higher than those of NVP/C. For NVP/C, the weight loss is derived from the decomposition of excessed citric acid. For other modified composites, the sluggish mass loss comes from the decomposition of carbon matrix materials and citric acid, coinciding with the preconceived strategy [55, 56]. The adequate carbon can construct a beneficial electronic conductive network to improve the rate capability of modified composites significantly.

Cyclic voltammetry (CV) measurement tested at a working window of 2.3–4.1 V with a scan rate of 0.1 mV s^{-1} is carried out to identify the electrochemical behaviors of all electrodes. As revealed in Fig. 6, all samples present the identical redox peaks, including oxidation peak at 3.54 V and divisive reduction peak at around 3.21 and 3.34 V. All existed peaks are corresponding to the V^{3+}/V^{4+} redox

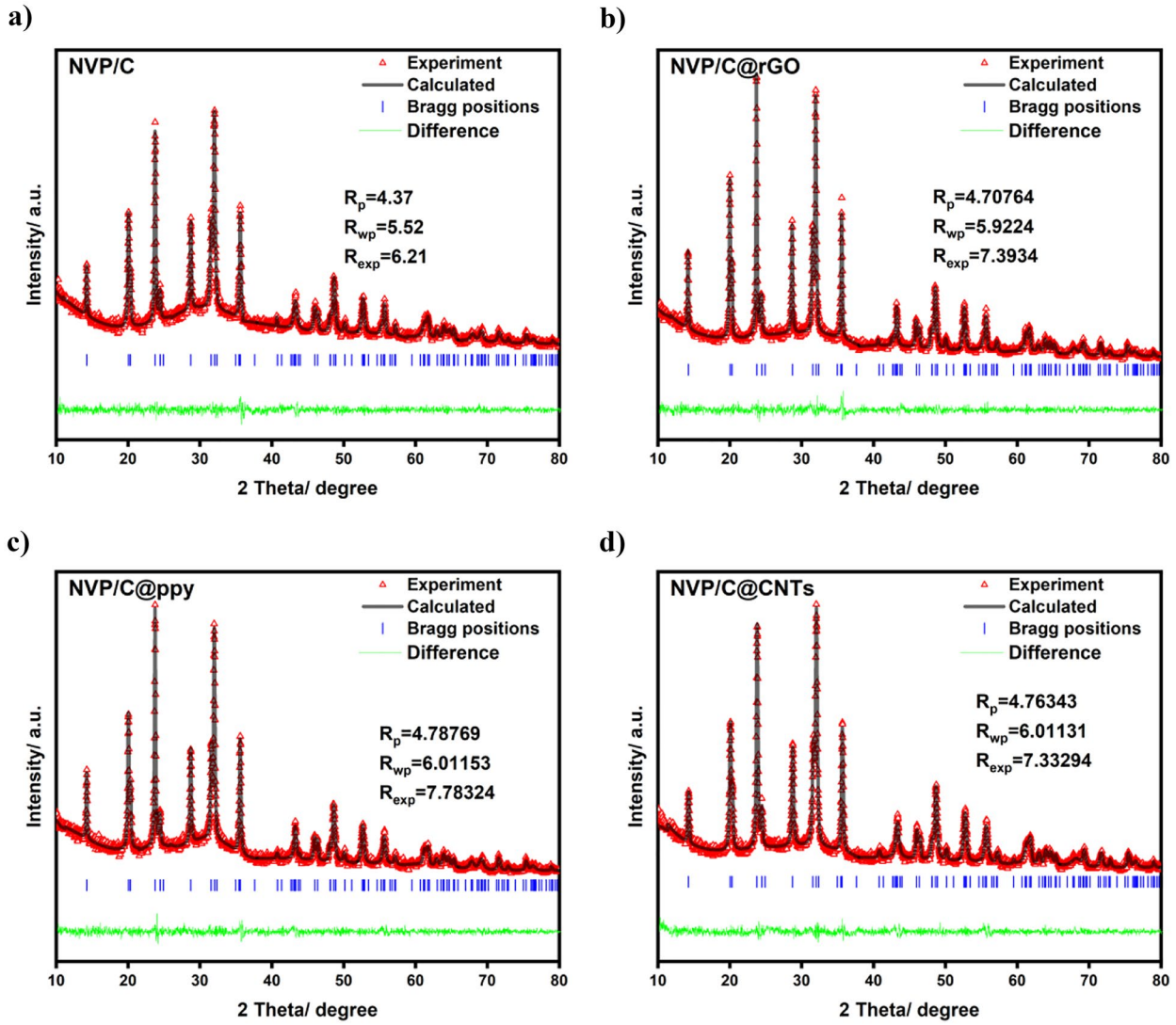

Fig. 2 Refined XRD patterns of all samples by Highscore software **a** NVP/C **b** NVP/C@rGO **c** NVP/C@ppy **d** NVP/C@CNTs

pair that occurred in the NVP system during the procedure of de-intercalation of Na^+. The split of the reduction peak may be resulted from the non-uniform distribution of particle size. Moreover, as for the discharge process, the scanning area for three carbonous composites is much larger than the NVP/C sample, suggesting that the modified samples possess more capacities. Meanwhile, these samples containing a carbon matrix behave stronger peak intensity, indicating the better Na^+ migration capability.

Furthermore, to deeply investigate the kinetic characteristics using CV measurement, all electrodes are tested at different scan rates of 0.1, 0.2, 0.5, 1, 2, and 5 mV s^{-1}. The results are displayed in Fig. 7. On the whole, for all composites, the polarization voltage obviously increases as the change of scan rate, indicating the worse reversibility along with the increase of scan rate. Interestingly, when the rate becomes higher, the divisive reduction peaks merge into one peak, suggesting that the two-step de-intercalation procedure has disappeared at high current rate. Furthermore, the apparent diffusion coefficient of Na^+ (D_{Na+}) can be calculated by the Randles–Sevcik equation as shown below [57, 58]:

Table 1 Refined crystal cell parameters for all samples

Sample	a/Å	b/Å	c/Å	V/Å^3
NVP/C	8.726	8.726	21.82	1439.18
NVP/C@CNTs	8.727	8.727	21.84	1439.74
NVP/C@rGO	8.725	8.725	21.83	1439.23
NVP/C@ppy	8.729	8.729	21.83	1440.32

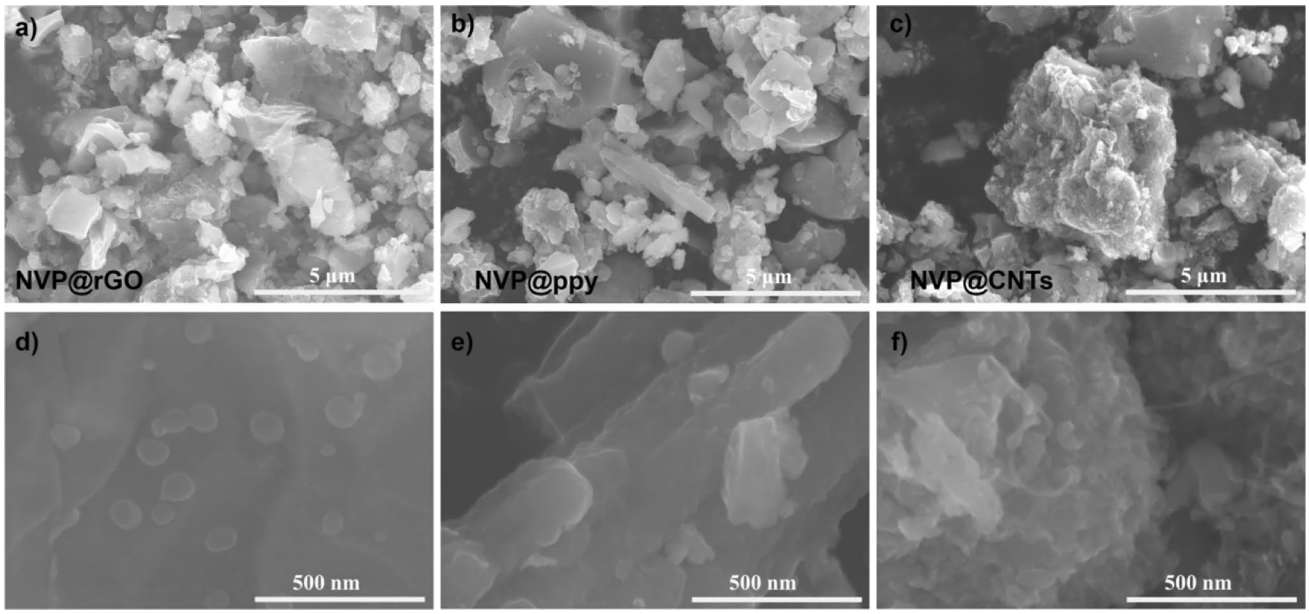

Fig. 3 SEM and HRSEM images of **a**, **d** NVP@rGO, **b**, **e** NVP@ppy, and **c**, **f** NVP@CNT samples

$$I_p = 2.69 \times 10^5 n^{3/2} A C D^{1/2} v^{1/2} \quad (1)$$

where n, A, C, and ν represent the number of transferred electrons ($n=2$), the contact area between cathode and electrolyte (here is 2.0096 cm^2), the concentration of Na^+ in the electrode (mol cm^{-3}), and scanning rate (V s^{-1}), respectively. Based on Eq. (1), we plot the curve containing the relationship between I_p and $v^{1/2}$. The slope values for all electrodes during charge and discharge process are revealed in Fig. 7b, d, f, h, and the obtained results are listed in Table 2. As shown in Table 2, all optimized samples containing the carbon matrix show a better D_{Na+} property than the NVP/C sample, suggesting that the conductive carbon matrix favors to facilitate the Na^+ migration effectively. Obviously, the NVP/C@CNT composite achieves the highest D_{Na+} values of 1.28×10^{-10} cm^2 s^{-1} and 8.56×10^{-11} cm^2 s^{-1} during the charge and discharge processes, demonstrating the superior kinetic characteristics.

Moreover, the controlling mode of all electrodes is evaluated by CV tests and the corresponding results are revealed in Fig. 8. As well known, we can acquire the controlling mode by the b-value (0.5 for the diffusion-controlled and 1 for the pseudocapacitance-controlled) according to the equation of $i = a\nu^b$, where i, v, and b represent the peak current,

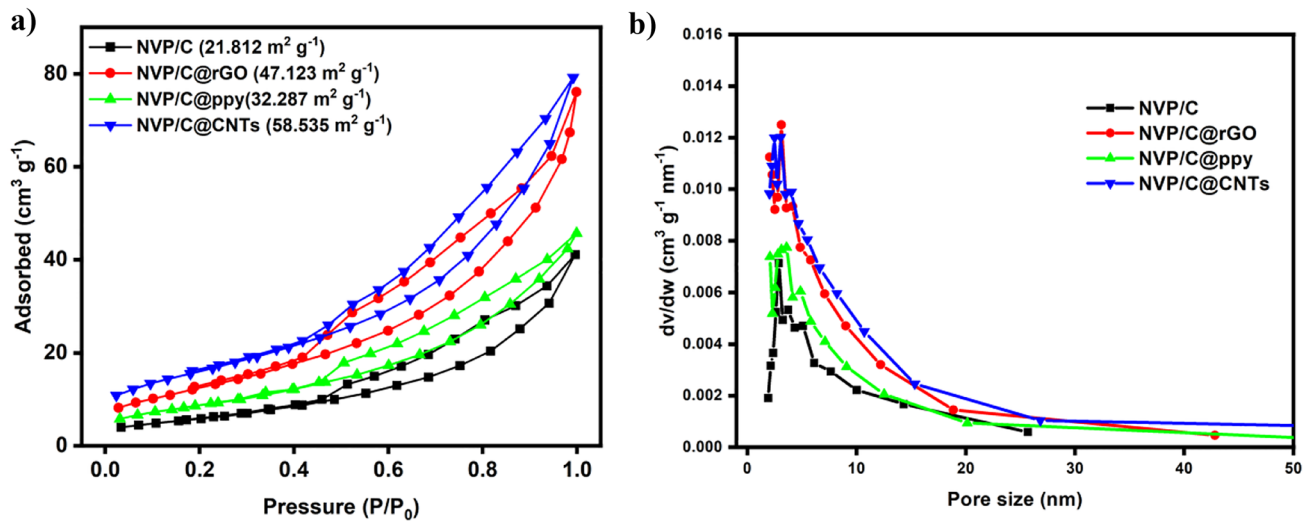

Fig. 4 **a** N2 absorption and desorption isotherm of all samples. **b** Barrett-Joyner-Halenda (BJH) pore distribution for all samples

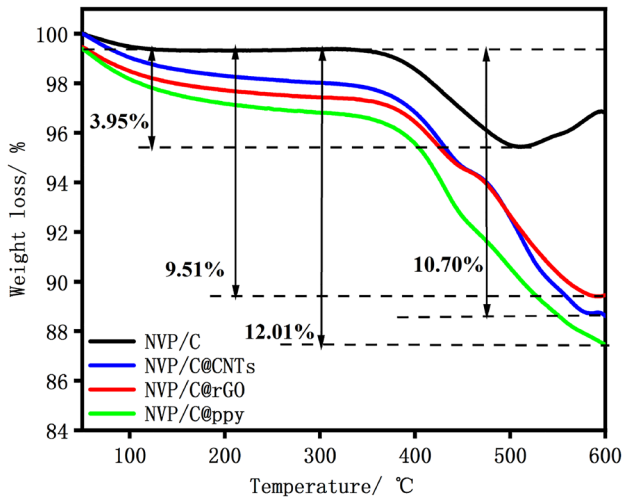

Fig. 5 TG curves of all samples conducted at the range of 50–600 °C

scan rate, and linear slope, respectively. As displayed in Fig. 8, the relationship between log*i* and log*v* is calculated and it behaves a linear correlation. According to the slope values, we can obtain the *b* values. Obviously, the *b* value for all samples during charge process is close to 0.5, indicating the controlling mode is diffusion-controlled. As for the discharge process, all samples reveal a *b* value of 0.9, suggesting a primary contribution of pseudocapacitance.

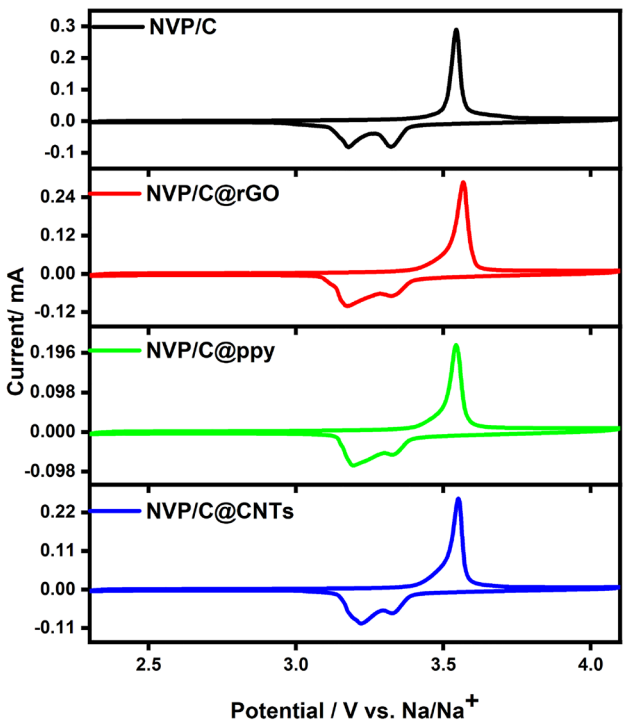

Fig. 6 Comparison of CV curves for all samples at a scan rate of 0.1 mV s^{-1}

Fig. 7 CV curves for **a** NVP/C, **c** NVP/C@rGO, **e** NVP/C@ppy, and **g** NVP/C@CNTs at 0.1, 0.2, 0.5, 1, 2, and 5 mV s^{-1}. The relationship between I_p and $v^{1/2}$ for **b** NVP/C, **d** NVP/C@rGO, **f** NVP/C@ppy, and **h** NVP/C@CNTs

To evaluate the sodium storage property of all electrodes, GCD measurements are carried out within a range of 2.3–4.1 V. Figure 9a shows the initial charge and discharge profiles of all samples at the 0.1 C rate. Clearly, all electrodes reveal a long and flat voltage plateau at 3.4 V, coinciding with the redox peaks presented in CV curves. This potential platform is derived from the redox reaction of V^{3+}/V^{4+}, corresponding to the phase reaction of $Na_3V_2(PO_4)_3$ and $Na_1V_2(PO_4)_3$. Specifically, the discharge capacities of NVP/C, NVP/C@rGO, NVP/C@ppy, and NVP/C@CNT composites are 85.6, 93.5, 97.8, and 98.8 mAh g^{-1}, respectively. It is demonstrated that adding a conductive carbon matrix is beneficial to improving the discharge capacity for the NVP system. Moreover, the polarization voltage is slight for all samples, indicating the excellent electrochemical reversibility. The rate capability for all composites is tested from 0.1 to 10 C, and the results are shown in Fig. 9b. Obviously, all modified samples containing carbon matrix materials possess higher specific capacities than the NVP/C sample at all different current densities. For the NVP/C@CNT electrode, the reversible capacities of 98.7, 89.3, 85.2, 83.2, 80.5, and 78.9 mAh g^{-1} are recorded at 0.1, 1, 2, 4, 6, and 10 C, respectively. The capacity retention can reach 80%. However, the corresponding reversible capacities of the NVP/C sample are 68.5, 63.8, 59.0, 56.9, 53.4, and 49.5 mAh g^{-1} at current densities of 0.1, 1, 2, 4, 6, and 10 C, respectively. The low retention ratio of 72.6% indicates the poor rate capability of NVP/C electrode. Significantly, other modified samples (NVP/C@rGO, NVP/C@ppy) reveal the similar rate performance as the NVP/C@CNT sample, suggesting that the addition of the conductive carbon-based matrix can greatly improve the rate performance.

The cycling performance of all composites at the 1 C rate is evaluated and displayed in Fig. 9c. The NVP/C sample delivers an original capacity of 72.5 mAh g^{-1} at 1 C, and a capacity of 65.6 mAh g^{-1} after 100 cycles. As for the modified samples, the reversible capacities are obviously superior than the NVP/C sample. Notably, the initial capacity of the NVP/C@CNT sample is 89.9 mAh g^{-1} and 93.4% capacity could be maintained after 100 cycles, indicating an enhanced cycling performance compared to NVP/C. Even after cycling for 300 cycles, a high capacity of 77.9 mAh g^{-1} can be obtained for NVP/C@CNTs. To explore the electrochemical reversibility, coulombic efficiency for NVP/C@CNTs is evaluated and shown in Fig. 9c. Obviously, the value can maintain at 100% during the prolonged process, indicating the excellent reversibility of the NVP/C@CNT electrode. At a higher rate of 2

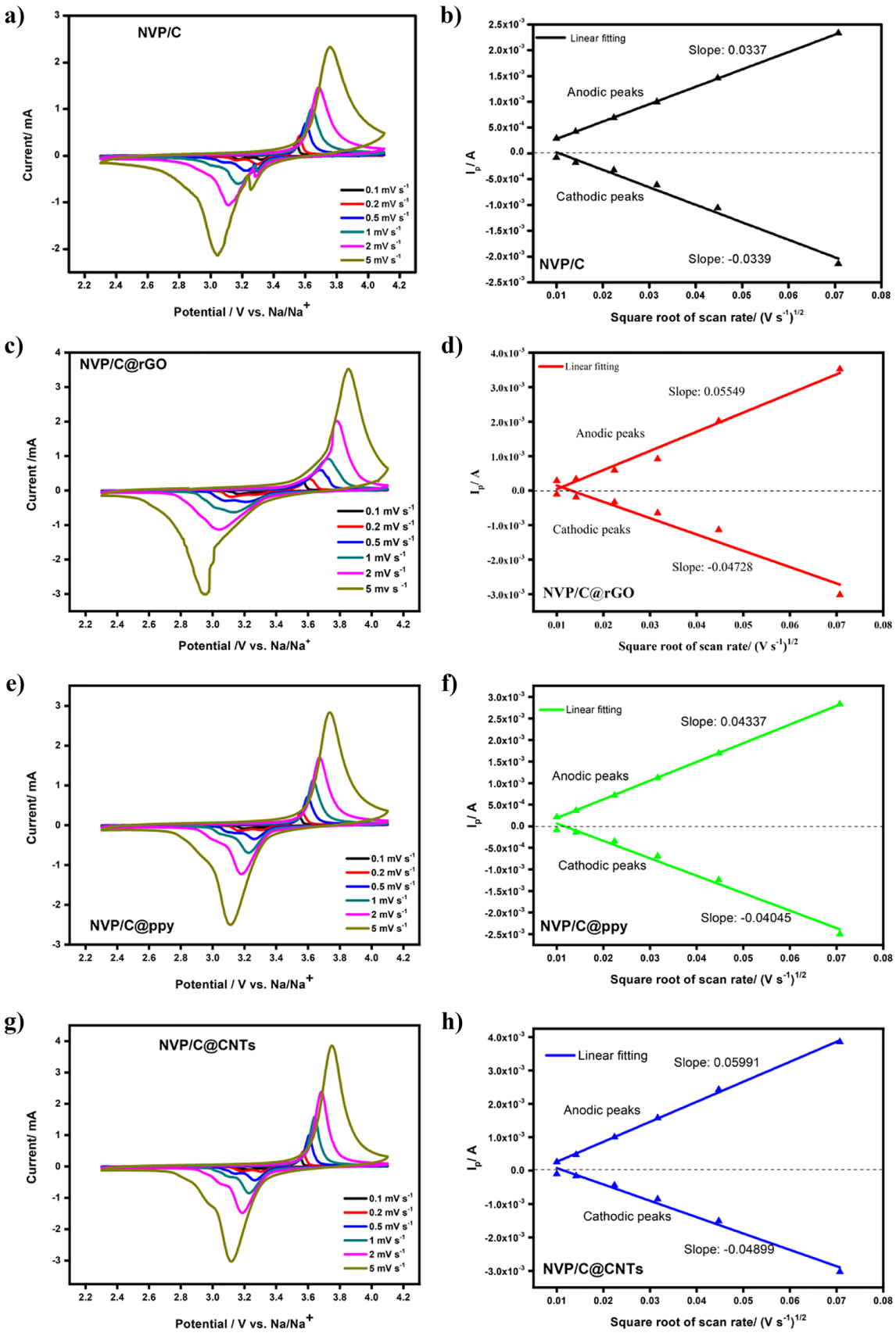
a)
NVP/C
Current/ mA
Potential / V vs. Na/Na+
0.1 mV s-1
0.2 mV s-1
0.5 mV s-1
1 mV s-1
2 mV s-1
5 mV s-1
b)
Linear fitting
Slope: 0.0337
Anodic peaks
Cathodic peaks
Slope: -0.0339
NVP/C
Ip/ A
Square root of scan rate/ (V s-1)1/2
c)
NVP/C@rGO
Current /mA
Potential /V vs. Na/Na+
d)
Linear fitting
Slope: 0.05549
Anodic peaks
Cathodic peaks
Slope: -0.04728
NVP/C@rGO
e)
NVP/C@ppy
f)
Slope: 0.04337
Slope: -0.04045
g)
NVP/C@CNTs
h)
Slope: 0.05991
Slope: -0.04899

Table 2 Apparent diffusion coefficients of Na^+ of all electrodes during charge and discharge

Sample	Slope		$D_{Na+}/cm^2\ s^{-1}$	
	Charge	Discharge	Charge	Discharge
NVP/C	0.0337	−0.0339	4.05×10^{-11}	4.10×10^{-11}
NVP/C@CNTs	0.05991	−0.04899	1.28×10^{-10}	8.56×10^{-11}
NVP/C@ppy	0.04337	−0.04045	6.71×10^{-11}	5.83×10^{-11}
NVP/C@rGO	0.05549	−0.04728	1.10×10^{-10}	7.97×10^{-11}

C, the NVP/C sample only delivers a reversible capacity of 68.7 mAh g^{-1} and remains a capacity of 57.9 mAh g^{-1} after 500 cycles. The optimized NVP/C@CNTs present the best cycling performance among all samples. It can release a high capacity of 91.5 mAh g^{-1} at the 1st cycle and keep a considerable value of 74.1 mAh g^{-1} after 500 cycles, suggesting a high capacity retention of 81%. Meanwhile, the coulombic efficiency of NVP/C@CNTs maintains close to 100% during the prolonged cycling process at 2 C, indicating the excellent reversibility of Na^+ insertion/extraction.

Moreover, the SEM images of NVP/C and NVP/C@CNT samples cycled at 1 C after 100 cycles are revealed in Fig. 10. As shown below, both composites display white particles and tiny black grains, which correspond to the PVDF binder and conductive agent acetylene, respectively. The tested powders originate from the electrode slice after cycling, which contains the active

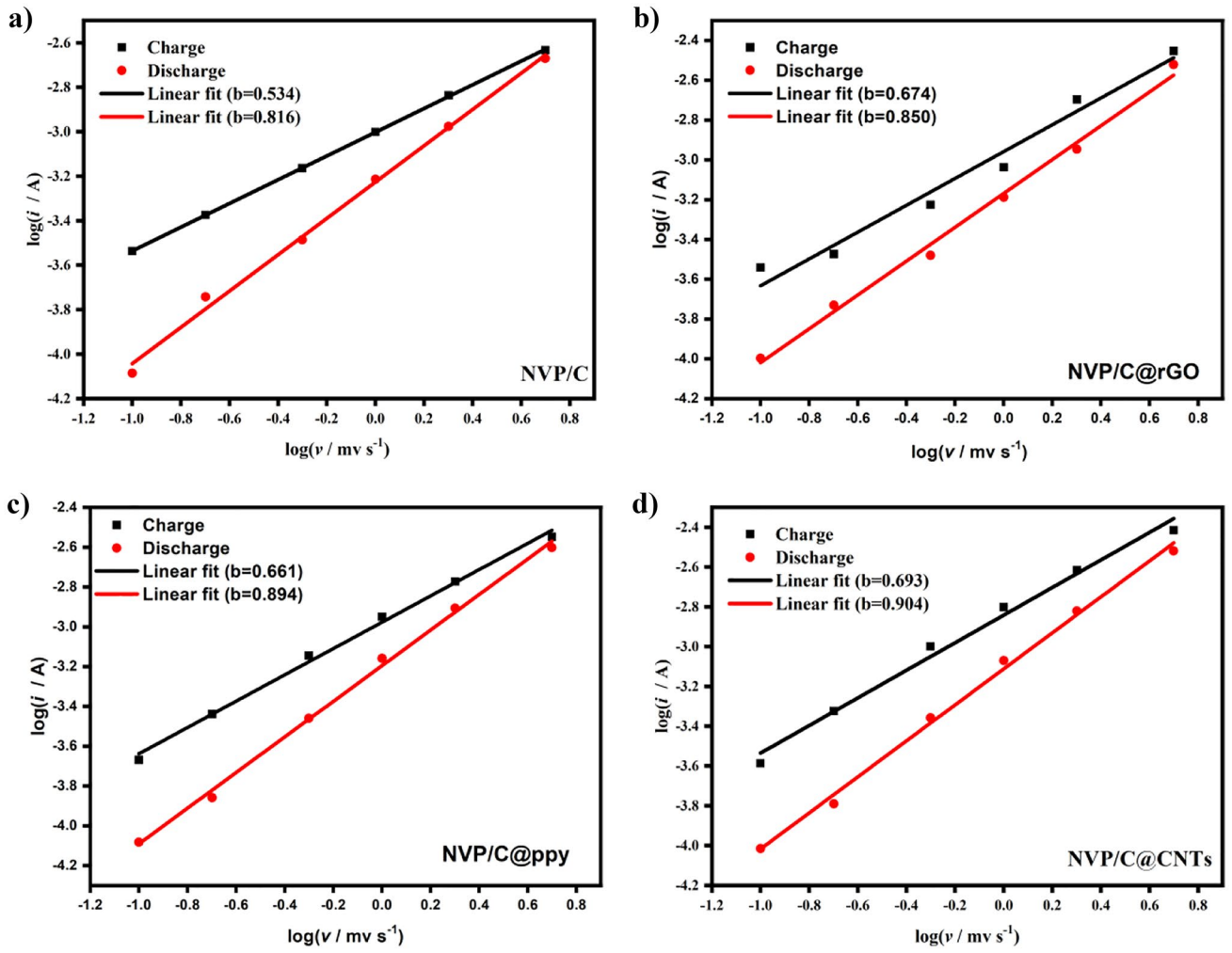

Fig. 8 The relationships between log (i) and log (v) from 0.1 to 5 mV s^{-1} for **a** NVP/C **b** NVP/C@rGO **c** NVP/C@ppy **d** NVP/C@CNTs

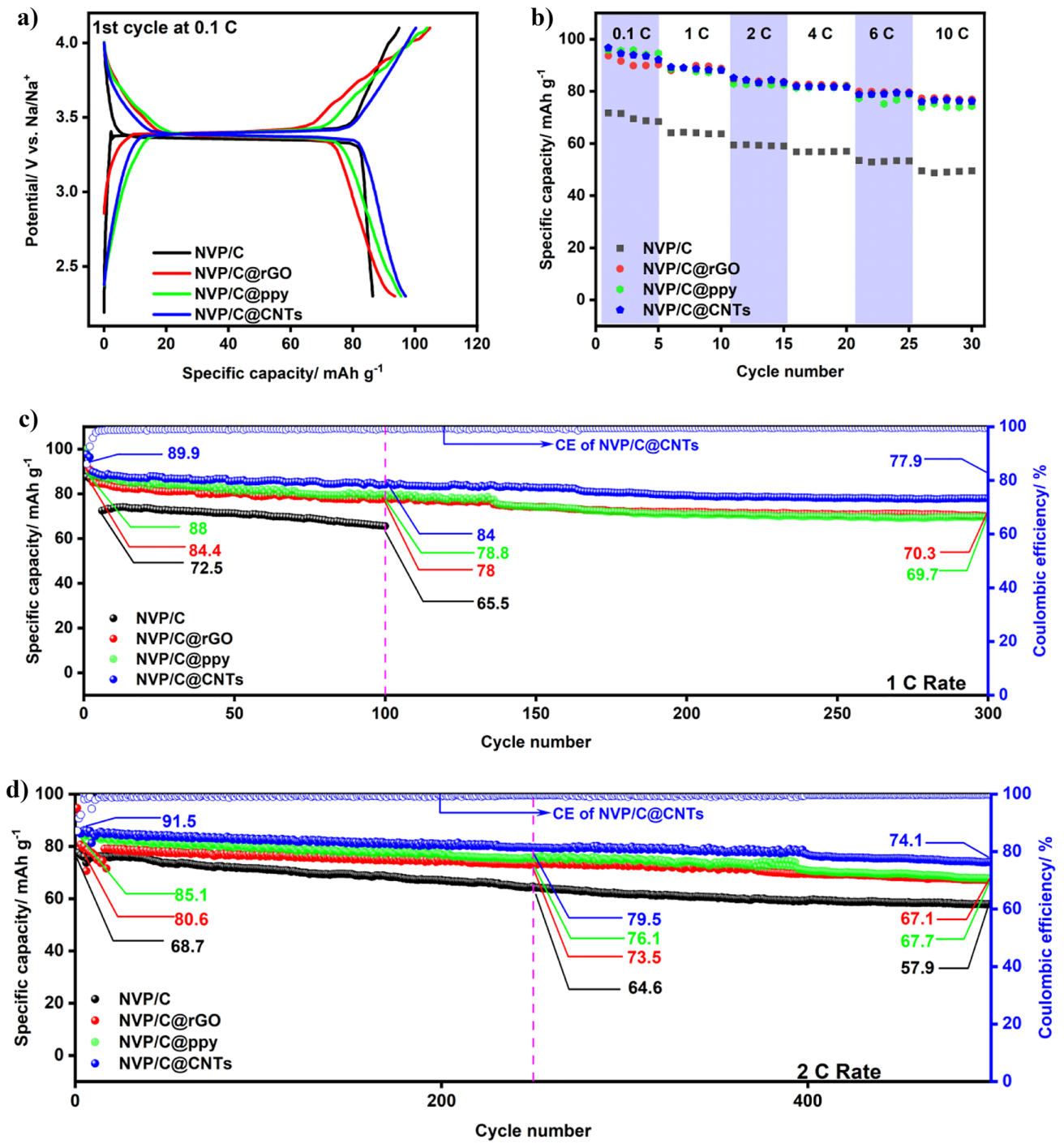

Fig. 9 Sodium storage property with voltage range of 2.3–4.1 V: **a** initial charge/discharge profiles, **b** rate capability of all samples, and cycling performance for all electrodes at the **c** 1 C and **d** 2 C rates

material, conductive agent, and binder. Figure 10a shows that severe agglomeration of active materials is emerged for the NVP/C sample after cycling, which may inferior electrochemical performance. However, the distribution of active grains is still homogeneous for the NVP/C@CNT composite reveled in Fig. 10b, demonstrating the stable structure, which results in the superior sodium storage property.

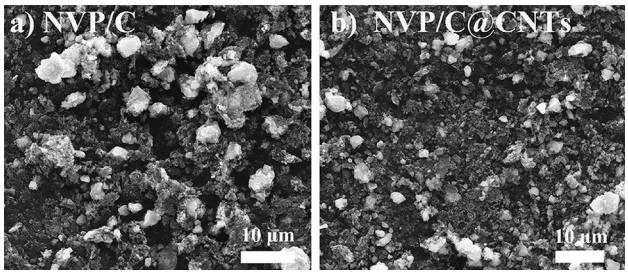

Fig. 10 SEM images of electrodes cycled at the 1 C rate after 100 cycles: **a** NVP/C and **b** NVP/C@CNTs

4 Conclusion

In conclusion, beneficial conductive carbon-based matrix materials are introduced into the NVP system to improve the kinetic characteristics and sodium storage properties. The modified samples are successfully synthesized by a facile sol–gel method. Notably, the NVP/C@CNT composite possesses the largest specific surface area and fastest Na^+ diffusion coefficient, revealing the superior rate capability and cycling performance. Distinctively, it can release reversible discharge capacities of 98.7, 89.3, 85.2, 83.2, 80.5, and 78.9 mAh g^{-1} at 0.1, 1, 2, 4, 6, and 10 C rates. A high capacity retention of 81% is obtained after 500 cycles at 2 C. Thus, the strategy of combining with conductive carbon-based matrix materials is a new mode for the development of cathode with enhanced electrochemical performance in SIBs.

Funding This work was supported by the National Key R&D Program of China (Project No. 2021YFE0104700), the Shanxi Province Science Foundation (Project No. 201901D111148), and the Science and Technology Project of State Grid Shanxi Electric Power Company (Project No. 52053018000 T).

Declarations

Conflict of interest The authors declare no competing interests.

References

1. Kretschmer K, Sun B, Zhang J, Xie X, Liu H, Wang G (2017) 3D Interconnected carbon fiber network-enabled ultralong life $Na_3V_2(PO_4)_3$ @Carbon paper cathode for sodium-ion batteries. Small 13(9):1603318. https://doi.org/10.1039/c9cp05559b
2. Li N, Tong Y, Yi D, Cui X, Zhang X (2020) 3D interconnected porous carbon coated $Na_3V_2(PO_4)_3$/C composite cathode materials for sodium-ion batteries. Ceram Int 46(17):27493–27498. https://doi.org/10.1021/acssuschemeng.8b06385
3. Liu J, Zhang L-L, Cao X-Z, Lin X, Shen Y, Zhang P, Wei C, Huang Y-Y, Luo W, Yang X-L, Han D-M (2020) Achieving the stable structure and superior performance of $Na_3V_2(PO_4)_2O_2F$ cathodes via Na-site regulation. ACS Applied Energy Materials 3(8):7649–7658. https://doi.org/10.1021/acsaem.0c01077
4. Zhang J, Liu W, Hu H, Li X, Huang Y, Chen T, Zhuo Y, Liu K (2018) An advanced blackberry-shaped $Na_3V_2(PO_4)_3$ cathode: assists in high-rate performance and long-life stability. Electrochim Acta 292:736–741. https://doi.org/10.1016/j.electacta.2018.10.007
5. Deokate R (2020) Chemically deposited $NiCo_2O_4$ thin films for electrochemical study, ES Mater Manuf 11: 16–19. https://doi.org/10.30919/esmm5f938
6. Wang Y, Liu Y, Wang C, Liu H, Zhang J, Lin J, Fan J, Ding T, Ryu J E, Guo Z (2020) Significantly enhanced ultrathin NiCo-based MOF nanosheet electrodes hybrided with Ti_3C_2Tx MXene for high performance asymmetric supercapacitors. Eng Sci 9: 50–59. https://doi.org/10.30919/es8d903
7. Patil S, Bhat T, Teli A M, Beknalkar S, Dhavale S, Faras M, Karanjkar M, Patil P (2020) Hybrid solid state supercapacitors (HSSC's) for high energy & power density: an overview. Eng Sci 12: 38–51. https://doi.org/10.30919/es8d1140
8. Dong H, Li Y, Chai H, Cao Y, Chen X (2019) Hydrothermal synthesis of CuCo S nano-structure and N-doped graphene for high-performance aqueous asymmetric supercapacitors. ES Energy Environ 4: 19–26. https://doi.org/10.30919/esee8c221
9. Sayyed S, Mahadik M, Shaikh A, Jang J, Pathan H (2019) Nanometal oxide based supercapacitor via electrochemical deposition. ES Energy Environ 3: 25–44. https://doi.org/10.30919/esee8c211
10. Rehman S, Ahmed R, Ma K, Xu S, Tao T, Aslam M, Amir M, Wang J (2020) Composite of strip-shaped ZIF-67 with polypyrrole: a conductive polymer-MOF electrode system for stable and high specific capacitance. Eng Sci 13: 71–78. https://doi.org/10.30919/es8d1263
11. Wang X, Zeng X, Cao D (2018) Biomass-derived nitrogen-doped porous carbons (NPC) and NPC/polyaniline composites as high performance supercapacitor materials. Eng Sci 1: 55–63. https://doi.org/10.30919/es.180325
12. Wu N, Bai X, Pan D, Dong B, Wei R, Naik N, Patil R, Guo Z (2020) Recent advances of asymmetric supercapacitors. Adv Mater Interfaces 8(1).https://doi.org/10.1002/admi.202001710
13. Peng Z, Jiang Q, Peng P, Li F (2020) NH_3-activated fullerene derivative hierarchical microstructures to porous Fe_3O_4/N-C for oxygen reduction reaction and Zn-air battery, Eng Sci 14: 27–38. https://doi.org/10.30919/es8d1311
14. Kabbour H, Coillot D, Colmont M, Masquelier C, Mentre O (2011) alpha-$Na_3M_2(PO_4)_3$ (M = Ti, Fe): absolute cationic ordering in NASICON-type phases. J Am Chem Soc 133(31):11900–11903. https://doi.org/10.1021/ja204321y
15. Hu P, Wang X, Wang T, Chen L, Ma J, Kong Q, Shi S, Cui G (2016) Boron substituted $Na_3V(P_{1-x}B_xO_4)_3$ cathode materials with enhanced performance for sodium-ion batteries. Adv Sci (Weinh) 3:1600112. https://doi.org/10.1002/advs.201600112
16. Park S, Park W, Sound harrajan V, Mathew V, Hwang J-Y, Kim J (2021) C-$Na_3V_{1.96}Fe_{0.04}(PO_4)_3/Fe_2P$ nanoclusters with stable charge-transfer interface for high-power sodium ion batteries. Chem Eng J 404:126974. https://doi.org/10.1016/j.cej.2020.126974
17. Yan L, Wang H, Huang D, Luo H (2018) Electrodes with high conductivities for high performance lithium/sodium ion batteries. Engineered Science 1:4–20
18. Zhang Y, Li X, Zhu T, Ma S, Li H, Sun G (2018) Facile fabrication hierarchical pore structure $Li_{1.2}Mn_{0.54}Ni_{0.13}Co_{0.13}$-xSrx$O_2$ nanofiber for high-performance cathode materials, ES Mater Manuf 3: 38–46. https://doi.org/10.30919/esmm5f201
19. Hou C, Wang B, Murugadoss V, Vupputuri S, Chao Y, Guo Z, Wang C, Du W (2020) Recent advances in Co3O4 as anode materials for high-performance lithium-ion batteries. Eng Sci 11: 19–30. https://doi.org/10.30919/es8d1128

20. Rosle MF, Najmi N, Ishak MI, Mohamad Saman M, Hashim AH (2019) Calcination effect on particle morphologies and electrochemical performances of $Na_3V_2(PO_4)_3$/C composites as cathode for sodium-ion batteries. Materials Today: Proceedings 16:1856–1863. https://doi.org/10.1016/j.matpr.2019.06.061
21. Liu X, Li M, Yang X, Zeng X, Wang H, Jiang H (2020) Carbon encapsulation and chlorine doping enable $Na_3V_2(PO_4)_3$ superior sodium ion storage properties as cathode material for sodium ion battery. Powder Technol 364:70–77. https://doi.org/10.1016/j.powtec.2020.01.055
22. Zhu C, Kepeng S, van Aken PA, Joachim M (2014) Carbon-coated $Na_3V_2(PO_4)_3$ embedded in porous carbon matrix: an ultrafast Na-storage cathode with the potential of outperforming Li cathodes. Nano Lett 14(4):2175–2180. https://doi.org/10.1021/nl500548a
23. Chen L, Zhong Z, Ren S, Han D-M (2020) Carbon-Coated $Na_3V_2(PO_4)_3$ Supported on multiwalled carbon nanotubes for half-/full-cell sodium-ion batteries. Energy Technol 8(3). https://doi.org/10.1002/ente.201901080.
24. Wang C, He Z, Xie X, Mai X, Li Y, Li T, Zhao M, Yan C, Liu H, Wujcik E K, Guo Z (2018) Controllable cross-linking anion exchange membranes with excellent mechanical and thermal properties. Macromolecular Mater Eng 303(3). https://doi.org/10.1002/mame.201700462
25. Wang Q, Zhang M, Zhou C, Chen Y (2018) Concerted ion-exchange mechanism for sodium diffusion and its promotion in $Na_3V_2(PO_4)_3$ framework. The Journal of Physical Chemistry C 122:16649–16654. https://doi.org/10.1021/acs.jpcc.8b06120
26. Li H, Wu C, Bai Y, Wu F, Wang M (2016) Controllable synthesis of high-rate and long cycle-life $Na_3V_2(PO_4)_3$ for sodium-ion batteries. J Power Sources 326:14–22. https://doi.org/10.1016/j.jpowsour.2016.06.096
27. Zhao L, Zhao H, Du Z, Wang J, Long X, Li Z, Świerczek K (2019) Delicate lattice modulation enables superior Na storage performance of $Na_3V_2(PO_4)_3$ as both an anode and cathode material for sodium-ion batteries: understanding the role of calcium substitution for vanadium. Journal of Materials Chemistry A 7:9807–9814. https://doi.org/10.1039/c9ta00869a
28. Chen M, Hua W, Xiao J, Cortie D, Guo X, Wang E, Gu Q, Hu Z, Indris S, Wang XL, Chou SL, Dou SX (2020) Development and investigation of a high-voltage cathode material for high-power sodium-ion batteries. Angew Chem Int Ed Engl 59(6):2449–2456. https://doi.org/10.1002/anie.201912964
29. Chotard JN, Rousse G, David R, Mentré O, Courty M, Masquelier C (2015) Discovery of a sodium-ordered form of $Na_3V_2(PO_4)_3$ below ambient temperature. Chem Mater 27(17):5982–5987. https://doi.org/10.1021/acs.chemmater.5b02092
30. Huang H, Luo S, Liu C, Yang Y, Zhai Y, Chang L, Li M (2019) Double-carbon coated $Na_3V_2(PO_4)_3$ as a superior cathode material for Na-ion batteries. Appl Surf Sci 487:1159–1166. https://doi.org/10.1016/j.apsusc.2019.05.224
31. Shen W, Li H, Guo Z, Wang C, Li Z, Xu Q, Liu H, Wang Y, Xia Y (2016) Double-nanocarbon synergistically modified $Na_3V_2(PO_4)_3$: an advanced cathode for high-rate and long-life sodium-ion batteries. ACS Appl Mater Interfaces 8(24):15341–15351. https://doi.org/10.1021/acsami.6b03410
32. Oh JAS, He H, Sun J, Cao X, Chua B, Huang Y, Zeng K, Lu L (2020) Dual-nitrogen-doped carbon decorated on $Na_3V_2(PO_4)_3$ to stabilize the intercalation of three sodium ions. ACS Applied Energy Materials 3(7):6870–6879. https://doi.org/10.1021/acsaem.0c00973
33. Chen Y, Xu Y, Sun X, Wang C (2018) Effect of Al substitution on the enhanced electrochemical performance and strong structure stability of $Na_3V_2(PO_4)_3$/C composite cathode for sodium-ion batteries. J Power Sources 375:82–92. https://doi.org/10.1016/j.jpowsour.2017.11.043
34. Li J, Cheng J, Chen Y, Wang C, Guo L (2020) Effect of K/Zr co-doping on the elevated electrochemical performance of $Na_3V_2(PO_4)_3$/C cathode material for sodium ion batteries. Ionics 27:181–190. https://doi.org/10.1007/s11581-020-03791-3
35. Zhang B, Zeng T, Liu Y, Zhang J (2018) Effect of Ti-doping on the electrochemical performance of sodium vanadium(iii) phosphate. RSC Adv 8(10):5523–5531. https://doi.org/10.1039/c7ra12743j
36. Li H, Yu X, Bai Y, Wu F, Wu C, Liu L, Yang X (2015) Effects of Mg doping on the remarkably enhanced electrochemical performance of $Na_3V_2(PO_4)_3$ cathode materials for sodium ion batteries. Journal of Materials Chemistry A 3(18):9578–9586. https://doi.org/10.1039/c5ta00277j
37. Zhang H, Hasa I, Buchholz D, Qin B, Passerini S (2017) Effects of nitrogen doping on the structure and performance of carbon coated $Na_3V_2(PO_4)_3$ cathodes for sodium-ion batteries. Carbon 124:334–341. https://doi.org/10.1016/j.carbon.2017.08.063
38. Gu E, Liu S, Zhang Z, Fang Y, Zhou X, Bao J (2018) An efficient sodium-ion battery consisting of reduced graphene oxide bonded $Na_3V_2(PO_4)_3$ in a composite carbon network. J Alloy Compd 767:131–140. https://doi.org/10.1016/j.jallcom.2018.07.082
39. Aparicio PA, Leeuw NH (2020) Electronic structure, ion diffusion and cation doping in the $Na_4VO(PO_4)_2$ compound as a cathode material for Na-ion batteries. Phys Chem Chem Phys 22(12):6653–6659. https://doi.org/10.1039/c9cp05559b
40. Luo L, Cheng B, Chen Y, Chen S, Liu G, Zhuo H (2020) Electrospun $Na_3V_2(PO_4)_3$/C nanofibers as self-standing cathode material for high performance sodium ion batteries. Materials Research Express 7:025508. https://doi.org/10.1088/2053-1591/ab6f37
41. Bi L, Li X, Liu X, Zheng Q, Lin D (2019) Enhanced cycling stability and rate capability in a La-doped $Na_3V_2(PO_4)_3$/C cathode for high-performance sodium ion batteries. ACS Sustainable Chemistry & Engineering 7(8):7693–7699. https://doi.org/10.1021/acssuschemeng.8b06385
42. Zheng W, Gao R, Zhou T, Huang X (2018) Enhanced electrochemical performance of $Na_3V_2(PO_4)_3$ with Ni^{2+} doping by a spray drying-assisted process for sodium ion batteries. Solid State Ionics 324:183–190. https://doi.org/10.1016/j.ssi.2018.07.006
43. Sadan MK, Kim H, Kim C, Cha SH, Cho KK, Kim K, Ahn J-H, Ahn H-J (2020) Enhanced rate and cyclability of a porous $Na_3V_2(PO_4)_3$ cathode using dimethyl ether as the electrolyte for application in sodium-ion batteries. Journal of Materials Chemistry A 8(19):9843–9849. https://doi.org/10.1039/d0ta02721a
44. Xiao H, Huang X, Ren Y, Wang H, Ding J, Zhou S, Ding X, Chen Y (2018) Enhanced sodium ion storage performance of $Na_3V_2(PO_4)_3$ with N-doped carbon by folic acid as carbon-nitrogen source. J Alloy Compd 732:454–459. https://doi.org/10.1016/j.jallcom.2017.10.195
45. Liu X, Feng G, Wu Z, Yang Z, Yang S, Guo X, Zhang S, Xu X, Zhong B, Yamauchi Y (2020) Enhanced sodium storage property of sodium vanadium phosphate via simultaneous carbon coating and Nb^{5+} doping. Chem Eng J 386:123953. https://doi.org/10.1016/j.cej.2019.123953
46. Yi H, Ling M, Xu W, Li X, Zheng Q, Zhang H (2018) VSC-doping and VSU-doping of $Na_3V_{2-x}Ti_x(PO_4)_2F_3$ compounds for sodium ion battery cathodes: analysis of electrochemical performance and kinetic properties. Nano Energy 47:340–352. https://doi.org/10.1016/j.nanoen.2018.02.053
47. Salehi AH, Masoudpanah SM, Hasheminiasari M, Yaghtin A, Safanama D, Ong CK, Reddy MV, Adams S (2020) A solution synthesis of $Na_3V_2(PO_4)_3$ cathode for sodium storage by using CTAB additive. Solid State Ionics 347:115269. https://doi.org/10.1016/j.ssi.2020.115269
48. Wu T, Sun J, Jeremy Yap Z Q, Ke M, Lim C Y H, Lu L (2020) Substantial doping engineering in $Na_3V_{2-x}Fe_x(PO_4)_3$ ($0 \le x \le 0.15$)

as high-rate cathode for sodium-ion battery. Mater Design 186:108287. https://doi.org/10.1016/j.matdes.2019.108287
49. Li X, Zhao W, Yin R, Huang X, Qian L (2018) A highly porous polyaniline-graphene composite used for electrochemical supercapacitors. Eng Sci 3:89–95. https://doi.org/10.30919/es8d743
50. Wu Z, Li L, Guo N, Yang R, Jiang D, Zhang M, Zhang M, Huang Y, Guo Z (2019) Effect of a vinyl ester-carbon nanotubes sizing agent on interfacial properties of carbon fibers reinforced unsaturated polyester composites, ES Mater Manuf 6:38–48. https://doi.org/10.30919/esmm5f601
51. Wu N, Hu Q, Wei R, Mai X, Naik N, Pan D, Guo Z, Shi Z (2021) Review on the electromagnetic interference shielding properties of carbon based materials and their novel composites: recent progress, challenges and prospects. Carbon 176:88–105.https://doi.org/10.1016/j.carbon.2021.01.124
52. Yang P, Zhao H, Yang Y, Zhao P, Zhao X, Yang L (2020) Fabrication of N, P-codoped Mo2C/carbon nanofibers via electrospinning as electrocatalyst for hydrogen evolution reaction. ES Mater Manuf 7: 34–39. https://doi.org/10.30919/esmm5f618
53. Chen J, Wang X, Huang Y, Lv S, Cao X, Yun J, Cao D (2018) Adsorption removal of pollutant dyes in wastewater by nitrogen-doped porous carbons derived from natural leaves. Eng Sci 5:30–38.https://doi.org/10.30919/es8d666
54. Lv Y, Zhu L, Xu H, Yang L, Liu Z, Cheng D, Cao X, Yun J, Cao D (2019) Core/shell template-derived Co, N-doped carbon bifunctional electrocatalysts for rechargeable Zn-air battery. Eng Sci 7: 26–37. https://doi.org/10.30919/es8d768
55. Hou C, Yang W, Xie X, Sun X, Wang J, Naik N, Pan D, Mai X, Guo Z, Dang F, Du W (2021) Agaric-like anodes of porous carbon decorated with MoO2 nanoparticles for stable ultralong cycling lifespan and high-rate lithium/sodium storage. J Colloid Interface Sci 596:396–407.https://doi.org/10.1016/j.jcis.2021.03.149
56. Hou C, Wang J, Du W, Wang J, Du Y, Liu C, Zhang J, Hou H, Dang F, Zhao L, Guo Z (2019) One-pot synthesized molybdenum dioxide–molybdenum carbide heterostructures coupled with 3D holey carbon nanosheets for highly efficient and ultrastable cycling lithium-ion storage. J Mater Chem A 7(22):13460–13472.https://doi.org/10.1039/C9TA03551F
57. Chen Y, Cheng J, He Z, Wang Y, Wang C, Guo L (2020) Silicon substituted $Na_3V_2(PO_4)_3$/C nanocomposites enwrapped on conducting graphene for high-rate and long-lifespan sodium ion batteries. Ceram Int 46(17):27660–27669. https://doi.org/10.1016/j.ceramint.2020.07.262
58. Luo C, Shen T, Ke B, Wu Y, Chen Y (2019) Ultra-small $Na_3V_2(PO_4)_3$ nanoparticles decorated MOFs-derived carbon enabling fast charge transfer for high-rate sodium storage. Solid State Ionics 342:115061. https://doi.org/10.1016/j.ssi.2019.115061